Temporal variations of atomic oxygen in the upper mesosphere from SABER

Anne K. Smith,[1] Daniel R. Marsh,[1] Martin G. Mlynczak,[2] and Jeffrey C. Mast[3]

Received 22 October 2009; revised 22 June 2010; accepted 29 June 2010; published 23 September 2010.

[1] One of the atmospheric constituents that can be retrieved from observations by the Sounding of the Atmosphere using Broadband Emission Radiometry (SABER) instrument on the Thermosphere-Ionosphere-Mesosphere Energetics and Dynamics (TIMED) satellite is atomic oxygen in the upper mesosphere. Atomic oxygen can be determined during both day and night using two different techniques that both rely on ozone chemistry. The O concentrations retrieved from SABER data are higher by a factor of 2–5 compared to concentrations determined from other measurements and techniques and compiled in current empirical models. This paper presents variability of atomic oxygen with a focus on the diurnal cycle in low latitudes and the seasonal cycle of daily mean atomic oxygen globally. The results show a large diurnal variation, ranging from a factor of 2 to more than a factor of 10, of atomic oxygen near the equator. The relative magnitude varies with season (larger near the equinoxes) and with altitude (largest near 85 km). Vertical transport by the migrating diurnal tide explains the observed variation. The semiannual variation in tidal amplitude affects the seasonal variation of daily average atomic oxygen, which likely indicates that there is irreversible transport by the tides. At high latitudes, the atomic oxygen variation is characterized by wintertime maxima over the altitude range 80–95 km and summertime maxima above. The wintertime peaks are associated with the downwelling from the mean circulation and are particularly strong in late winter of 2004, 2006, and 2009, responding to the unusual dynamical situations in those years.

Citation: Smith, A. K., D. R. Marsh, M. G. Mlynczak, and J. C. Mast (2010), Temporal variations of atomic oxygen in the upper mesosphere from SABER, *J. Geophys. Res.*, *115*, D18309, doi:10.1029/2009JD013434.

1. Introduction

[2] In the MLT (mesosphere-lower thermosphere), atomic oxygen (*O*) is the most abundant reactive trace species during both day and night. Its lifetime varies sharply with altitude and ranges from seconds at 50 km to months at 100 km. Where the lifetime is long, seasonal and latitudinal variations in *O* result from transport by waves, by the mean circulation, and by diffusion, as well as from photochemical production and loss. There are also shorter-term variations. For example, even though atomic oxygen has quite a long photochemical lifetime in the upper mesosphere, its concentration has a diurnal cycle [e.g., *Melo et al.*, 2001; *Russell et al.*, 2005]. In the MLT, there are large-scale large-amplitude dynamical variations associated with atmospheric tides. At low latitudes, the temperature amplitude of the monthly mean zonal average diurnal tide can be as large as 25 K; the tidal amplitude at some longitudes or globally for shorter periods can be higher. The tidal amplitudes also have marked semiannual and annual variations [*Xu et al.*, 2009].

[3] The Sounding of the Atmosphere using Broadband Emission Radiometry (SABER) instrument on the Thermosphere-Ionosphere-Mesosphere Energetics and Dynamics (TIMED) satellite makes measurements that can be used to determine atomic oxygen in the MLT [*Russell et al.*, 1999]. The techniques are different during day and night although both rely on the assumption that ozone is in photochemical equilibrium. During day, atomic oxygen is determined directly from the ozone. This study uses ozone retrieved from the 9.6 μm emission and therefore avoids the concerns about long radiative lifetime that apply to previous analyses that retrieve ozone from the $O_2(^1\Delta)$ 1.27 μm emission. At night, atomic oxygen is calculated from the Meinel bands airglow emission from vibrationally excited hydroxyl (*OH*). There are uncertainties in both the day and night retrievals due to uncertainties in some of the important input parameters. However, the excellent consistency between the day and night atomic oxygen lends confidence to the methods used.

[1]Atmospheric Chemistry Division, National Center for Atmospheric Research, Boulder, Colorado, USA.
[2]NASA Langley Research Center, Hampton, Virginia, USA.
[3]Science Systems and Applications Inc., Hampton, Virginia, USA.

0148-0227/10/2009JD013434

[4] The orbit of the TIMED satellite precesses in local time. Every 60–65 days, a yaw maneuver is performed to keep sunlight out of the SABER field of view. Over each of the intervening yaw periods, the SABER sampling covers almost 24 h of local time. There are thus six periods during each year during which we can construct the daily mean or diurnally varying behavior of atomic oxygen, temperature, and other retrieved quantities. This pattern repeats and similar data are now available for 46 yaw periods over more than 7 years.

[5] The results show that the atomic oxygen concentrations and variability are very consistent between day and night. Above about 83 km, short-term transport by the tidal vertical wind appears to account for the full extent of the diurnal variation. Even where the variation is controlled only by transport, the magnitude of the diurnal variation can be large. In the tropics, the magnitude of the *O* changes due to tidal transport can exceed an order of magnitude in the period near the vernal equinox when the amplitude of the migrating diurnal tide is largest.

2. Determination of Atomic Oxygen

[6] This section describes the basic process for determining atomic oxygen from SABER data. The methods are based on those that were developed by the SABER team for a standard atomic oxygen product [*Mlynczak*, 1999]. More details on the proposed operational retrieval will be presented in a paper by M. G. Mlynczak et al. (submitted manuscript, 2010). The atomic oxygen had been included in some v1.07 Level 2 files using the algorithm and rate coefficients that were used in earlier versions of the SABER data (v1.06 and earlier). The team has made a number of improvements to the algorithm that have significantly improved the stability and reliability of the retrieval. As a consequence, the older oxygen data has been removed from the version 1.07 SABER data files; oxygen profiles from the new retrieval will appear in future releases.

[7] The basic principles for determining day and night atomic oxygen are not new. The method of determining daytime *O* from O_3 using the assumption of photochemical equilibrium was presented by *McDade et al.* [1985], *Evans et al.* [1988], *Llewellyn et al.* [1993], *Llewellyn and McDade* [1996], and *Mlynczak et al.* [2007]. *Good* [1976] was the first to use observations of the *OH* Meinel band to determine nighttime atomic oxygen. The technique was expanded by *McDade and Llewellyn* [1988], who investigated the impact of uncertainties due to unknown parameters in the formulation of the emissions that make up the bands. The method of determining *O* concentration from satellite profiles of hydroxyl airglow during night has been discussed by *Mlynczak et al.* [1998], *Mlynczak* [1999] and *Russell and Lowe* [2003]. Techniques for determining *O* from other emissions, either alone or in conjunction with Meinel band emissions, provide additional sources of data [e.g., *Offermann*, 1972; *Offermann and Drescher*, 1973; *Melo et al.*, 2001; *Iwagami et al.*, 2003; *Russell and Lowe*, 2003; *Hecht et al.*, 2004].

[8] There are a number of details of the *O* retrieval that are unique to the SABER analysis. These are described here.

2.1. Algorithm for Retrieving *O*

[9] The determination of atomic oxygen in the upper mesosphere during day and night uses ozone photochemistry. The photochemical equations that are relevant are

$$O + O_2 + M \rightarrow O_3^* + M \quad \left(k_1 = 6.0 \times 10^{-34}(300/T)^{2.4}\right) \quad (1a)$$

$$H + O_3 \rightarrow OH^* + O_2 \quad \left(k_2 = 1.4 \times 10^{-10}\exp(-470/T)\right) \quad (1b)$$

$$O + O_3 \rightarrow O_2 + O_2 \quad \left(k_3 = 8.0 \times 10^{-12}\exp(-2060/T)\right) \quad (1c)$$

$$O_3 + h\nu \rightarrow O_2^* + O^* \qquad (J_{o_3}). \quad (1d)$$

[10] The asterisks indicate that the product is, or sometimes is, in an excited state. Reaction rates are from *Sander et al.* [2006].

[11] Ozone is produced from atomic oxygen by reaction (1a) and is destroyed by reactions (1b), (1c), and (1d). The lifetime of ozone above 80 km is very short during both day and night (minutes or shorter) so it is a good approximation to assume photochemical equilibrium between O_3 and *O* [*Smith and Marsh*, 2005]. During the day, the loss rate due to photolysis (1d) is so rapid that loss due to kinetic reactions can be neglected. Equating the daytime production and loss of ozone (in terms of number density) gives

$$k_1 \cdot [O] \cdot [O_2] \cdot n = J_{o_3} \cdot [O_3] \quad (2)$$

and therefore

$$[O]_{day} = \frac{J_{O_3} \cdot [O_3]}{k_1 \cdot [O_2] \cdot n}, \quad (3)$$

where n is the number density of the background atmosphere and the square brackets indicate number density of chemical species. Note that k_1 decreases with temperature. On a pressure surface, the number density n also decreases with temperature ($n = p/kT$ where p is pressure, T is temperature, and k is the Boltzmann constant).

[12] At night, the losses of ozone are not measured directly but can be determined from the Meinel band emission measured by SABER. During night, chemical equilibrium of ozone gives

$$k_1 \cdot [O] \cdot [O_2] \cdot n = (k_2 \cdot [H] + k_3 \cdot [O]) \cdot [O_3]. \quad (4)$$

The leading loss rate for upper mesospheric ozone is the reaction with hydrogen (1b). A product of this reaction is vibrationally excited hydroxyl (*OH**). We define P_{OH*} as the rate of production of vibrationally excited *OH* at all vibrational levels,

$$P_{OH*} = k_2 \cdot [H] \cdot [O_3]. \quad (5)$$

SABER measures the 2.0 μm emission, which is emitted by the *OH** vibrational transitions 9–7 and 8–6 (i.e., the decay

Table 1. Parameters in the OH Emission Model Used in the Nighttime Retrieval of Atomic Oxygen

Parameter	Description	Value	Units
k_9^{O2}	Collisional removal of OH(9) by O_2	3 e-11	$cm^3\ s^{-1}$
k_9^{N2}	Total rate of collisional removal of OH(9) by N_2	4.0 e-13	$cm^3\ s^{-1}$
k_8^{O2}	Total rate of collisional removal of OH(8) by O_2	1.19 e-11	$cm^3\ s^{-1}$
k_8^{N2}	Total rate of collisional removal of OH(8) by N_2	7.0 e-13	$cm^3\ s^{-1}$
k_9^O	Total rate of removal of OH(9) by atomic oxygen	5 e-11	$cm^3\ s^{-1}$
k_8^O	Total rate of removal of OH(8) by atomic oxygen	5 e-11	$cm^3\ s^{-1}$
k_{98}^{O2}	Rate of collisional quenching of OH(9) to OH(8) by O_2	4.2 e-12	$cm^3\ s^{-1}$
k_{98}^{N2}	Rate of collisional quenching of OH(9) to OH(8) by N_2	4.0 e-13	$cm^3\ s^{-1}$
A_9	Inverse radiative lifetime for OH(9)	215.05	s^{-1}
A_8	Inverse radiative lifetime for OH(8)	178.06	s^{-1}
A_{97}	Radiative lifetime for the OH(9–7) transition	118.35	s^{-1}
A_{86}	Radiative lifetime for the OH(8–6) transition	117.21	s^{-1}

from level 9 to level 7 and from level 8 to level 6). The net retrieved volume emission rate *VER* is

$$VER = E_{97}A_{97}n_9 + E_{86}A_{86}n_8, \tag{6}$$

where E_{ij} and A_{ij} are the photon energies and spontaneous emission rates (Einstein coefficients) for the *i–j* vibrational transition.

[13] Due to the limited energy available from the exothermic reaction (1b), the highest vibrational level populated is $v = 9$. Assuming the hydroxyl states are in equilibrium, the number density of the population is

$$n_i = \frac{P_i}{L_i}, \tag{7}$$

where P_i and L_i are production and loss of the *i*th vibrational level. Loss of [*OH**] includes spontaneous emission of radiation as quantified by the Einstein coefficients, quenching by collision with O_2 or N_2, and reaction with or quenching by atomic oxygen,

$$L_i = A_i + k_i^{O_2} \cdot [O_2] + k_i^{N_2} \cdot [N_2] + k_i^O \cdot [O]. \tag{8}$$

P_9 includes only direct population by reaction (1b) while P_8 includes both direct population and cascade from level P_9. f_i is the branching ratio for the *i*th level in (1a), so that $P_9 = f_9 P_{OH*}$ and $P_8 = f_8 P_{OH*} + n_9\ (A_{98} + k_{98}^{O_2}[O_2] + k_{98}^{N_2}[N_2])$ or $P_8 = [f_8 + f_9/L_9\ (A_{98} + k_{98}^{O_2}[O_2])] + k_{98}^{N_2}[N_2]P_{OH*}$.

[14] Applying (6) and (7) gives

$$VER = \left\{ E_{97}A_{97}\frac{f_9}{L_9} + E_{86}A_{86}\frac{\left[f_8 + \frac{f_9\left(A_{98} + k_{98}^{O_2}[O_2] + k_{98}^{N_2}[N_2]\right)}{L_9}\right]}{L_8} \right\} \cdot P_{OH*}. \tag{9}$$

From (4) and (5),

$$[O]_{night} = \frac{k_2 \cdot [H] \cdot [O_3]}{(k_1 \cdot [O_2] \cdot n - k_3 \cdot [O_3])} = \frac{P_{OH*}}{(k_1 \cdot [O_2] \cdot n - k_3 \cdot [O_3])}. \tag{10}$$

With the substitution of P_{OH*} from (9) into (10), we can derive [*O*] from *VER*. The vibrational level loss rates L_8 and L_9 include atomic oxygen; to actually solve (10) we express it as a quadratic equation in atomic oxygen.

[15] A factor that has hampered efforts to use the Meinel emissions to deduce properties of the mesosphere is the uncertainty in many of the physical coefficients and parameters involved in the transitions. While SABER is not immune from this, the experiment was designed to minimize the impacts of these on the investigation of the MLT region. The SABER 2.0 μm *OH* channel was chosen specifically because the analysis is more straightforward if it uses emissions from the $v = 9$ and $v = 8$ states of *OH*, which are formed directly as a product of the reaction of atomic hydrogen and ozone. This facilitates the derivation of the rates of heating due to this reaction, as well as the derivation of atomic oxygen and atomic hydrogen, since it minimizes the number of kinetic rate coefficients and radiative lifetimes needed. In addition, the parameters that are required are typically the total rate of removal of the $v = 9$ and $v = 8$ states, i.e., state-to-state rate coefficients and radiative transition probabilities are not essential. The key rate coefficients are those for collisional removal of the $v = 9$ and $v = 8$ states ($k_9^{O_2}k_9^{N_2}$, etc.) the rates for the downward cascade from $v = 9$ to $v = 8$ by emission or collisional quenching (A_{98}, $k_{98}^{O_2}$, $k_{98}^{N_2}$, etc.), the inverse radiative lifetimes of the $v = 9$ and $v = 8$ states (A_9, A_8) and the inverse radiative lifetimes for the 9–7 and 8–6 transitions (A_{97}, A_{86}). Table 1 gives a list of the main parameters used in this analysis.

[16] The collision quenching rates for $v = 9$ and $v = 8$ by O_2 and N_2 are consistent with those found by *Adler-Golden* [1997]. The inverse radiative lifetimes (i.e., Einstein coefficients for spontaneous emission of radiation) are derived from the dipole moment measurements reported by *Nelson et al.* [1990] and were provided to the SABER project by David Nesbit [D. Nesbit, Joint Institute for Laboratory Astrophysics, private communication, 1990]. The values are in excellent agreement with those recently reported by *van der Loo and Groenenboom* [2007] in a theoretical calculation.

[17] The last rate coefficients to discuss are those involving collisions between atomic oxygen and vibrationally excited *OH*($v = 9$) and *OH*($v = 8$). The value that is required for the SABER model is the total rate of removal of these states. It does not matter whether the removal proceeds through collisional quenching (in which the *OH* molecule remains in a lower quantum state) or whether the process proceeds by chemical reaction, destroying the excited *OH* molecule. The question of the vibrational dependence of the rate of removal of *OH*(v) by atomic oxygen has been an issue for some time. *Spencer and Glass* [1977] report that the value for the removal of *OH*($v = 1$) is about twice that for the reaction of ground state *OH* with *O*. In developing the SABER algorithm, a value of 5×10^{-11} $cm^3\ s^{-1}$, which is about twice the rate for reaction of the ground state of OH with

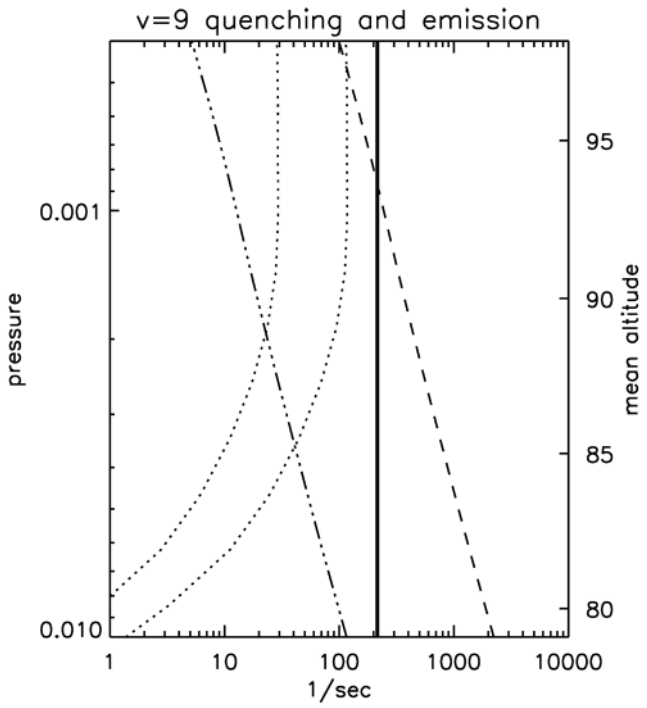

Figure 1. Profiles of the terms contributing to the loss of $OH(v = 9)$. Solid: A_9; dashed: $k_9^{O_2}$ $[O_2]$; dot-dashed: $k_9^{N_2}$ $[N_2]$; and dotted: $k_9^O \cdot [O]$ with two different options for k_9^O.

atomic oxygen at mesospheric temperatures, is adopted for $OH(v = 9)$ and $OH(v = 8)$. Testing of a larger rate of ($\sim 3 \times 10^{-10}$ cm^3 s^{-1}), reported by *Copeland et al.* [2006] from laboratory measurements, was found to give unphysically large values of atomic oxygen, energy deposition, and heating rates, as reported by M.G. Mlynczak (Atomic oxygen, atomic hydrogen, and chemical heating rates derived from SABER, paper presented at the 38th COSPAR Scientific Assembly, Montreal, Canada, 2008). Because of the uncertainties in the rates and in the products of the quenching and/or reaction, collisional quenching by O for the transition from $OH(v = 9)$ to $OH(v = 8)$, i.e., k_{98}^O, is not included.

[18] The details of the quenching rates can be important for the O retrieval when they have magnitudes comparable to the spontaneous emission rate. By increasing the rates of removal of $OH(v)$ by quenching, the derived production of OH (P_{OH*}) must increase to maintain balance. Since we are assuming photochemical balance between P_{OH*} and the recombination of atomic and molecular oxygen (1a), the algorithm must produce more atomic oxygen to account for this. Thus, increased quenching of $OH(v)$ yields increased amounts of atomic oxygen.

[19] Figure 1 shows the rates for removal of $OH(v = 9)$ by A_9, $k_9^{O_2} \cdot [O_2]$, $k_9^{N_2} \cdot [N_2]$, and $k_9^O \cdot [O]$ with two different values of k_9^O. The slower removal profile uses the value of k_9^O that we used in the retrievals ($k_9^O = 5 \times 10^{-11}$) and the faster removal rate uses $k_9^O = 2 \times 10^{-10}$. Quenching by collision with O_2 is the largest loss except in the uppermost part of the region plotted, where emission becomes larger. With the faster rate for k_9^O, the quenching by, or reaction with, O becomes competitive with the quenching by O_2. Comparisons of the retrieved O using these rates are presented in section 3.

2.2. Data and Other Input

[20] The SABER data used are from version 1.07, Level 2A of the operational SABER data set. The data products used are temperature, day and night ozone from the 9.6 μm retrieval, and volume emission rate of hydroxyl emission at 2.0 μm. The hydroxyl volume emission rate used is the one that has been "unfiltered" (OH_20_ver_unfilt in the SABER Level 2 files) to account for the truncation of the signal due to the width of the filter. Data cover the period from 25 January 2002 through 15 September 2009. The data are flagged as day, night, or twilight. The twilight flag refers to cases in which the atmosphere is partially illuminated. The retrieval algorithms are different during day and night; neither is completely appropriate for twilight. Due to the unknown but possibly increased uncertainty in the retrievals during twilight, we do not use these data.

[21] The results presented in this paper use data analyzed over entire yaw periods. The dates of the yaws (which vary slightly from year to year) are given in Table 2. See http://www.timed.jhuapl.edu/WWW/mission/yaws/yaws.app for the exact date and time of each yaw maneuver.

[22] A description of the non-LTE inversion of the CO_2 infrared emissions to obtain temperature and comparisons with other data are given by *Mertens et al.* [2001, 2004, 2008], *Kutepov et al.* [2006], *Oberheide et al.* [2006], and *Remsberg et al.* [2008]. *Remsberg et al.* [2008] report that agreement between SABER temperature and that from several ground-based techniques in the MLT region is within the mutual uncertainties. The SABER retrieval involves a complex non-LTE model with 133 vibrational states. Atomic oxygen is an important quencher in the thermosphere but plays a lesser role in the upper mesosphere. According to quantitative testing reported by *Mertens et al.* [2001], a 50% increase or decrease in O at 96 km would lead, respectively, to a 1.2 K decrease or 3.6 K increase in the retrieved T. The impact drops rapidly below this altitude. The uncertainty in the T retrieval in the mesosphere due to quenching by O is less than the noise in the measurement.

[23] In the v1.07 temperature retrieval, daytime atomic oxygen between 80 and 95 km was determined from the SABER ozone, using the technique described in equation (3) except that the 1.27 μm version of the ozone was used [*Remsberg et al.*, 2008]. Above 95 km during day and at all levels during night, atomic oxygen is specified from the NRL-MSIS model [*Picone et al.*, 2002]. Seasonal and latitudinal variations of O are included in the NRL-MSIS atomic oxygen but there are no diurnal variations. This means

Table 2. Range of Values for the Day of Year of SABER Yaw Maneuvers[a]

North Looking		South Looking	
Begin	End	Begin	End
11–15	75–78	75–78	138–142
138–142	194–198	194–198	258–263
258–263	322–325	322–325	11–15

[a]These mark the beginning and end of the SABER yaw periods over the period January 2002 through September 2009.

that the *O* concentrations that are used in the retrievals of nighttime temperature will not vary due to tides and other dynamical perturbations, which could have an impact on the retrieved profiles. As noted above, the impact of *O* on the temperature retrieval is small below 100 km and therefore probably is not an important factor in the results presented here. A primary effect of the specified climatological *O* is to reduce the profile-to-profile variability in temperature.

[24] The 9.6 μm emission used to retrieve day and night ozone is also not in local thermodynamic equilibrium. This ozone product is used during both day and night. An alternative ozone product is available during the day, using the 1.27 μm emission from $O_2(^1\Delta)$ [*Mlynczak et al.*, 2007]. The 1.27 μm emission can deviate fairly significantly from equilibrium, especially after sunrise or in the presence of strong vertical motions [*Zhu et al.*, 2007]. In the present analysis the 9.6 μm ozone is used for the daytime *O* retrieval.

[25] Photolysis of ozone is calculated from the TUV model [*Madronich and Flocke*, 1998]. Since there is very little ozone above the mesosphere, the atmosphere is optically thin at the ultraviolet wavelengths that are important and the ozone photolysis rate is nearly constant. The photolysis cross-sections for ozone have a temperature dependence over part of the ultraviolet frequency range; this effect applies for wavelengths longer than 260 nm but is relatively small for wavelengths less than 290–300 nm [*Sander et al.*, 2006]. This part of the spectrum has minimal impact on photolysis in the upper mesosphere so, in the calculations, we neglect temperature dependence of J_{O3}. There is a small bias introduced because a mean solar flux is used for the calculations reported here. In reality the flux decreases over this period due to the declining phase of the solar cycle. Ozone photolysis is dominated by the Hartley bands, which vary by ~1%–2% over the solar cycle [e.g., *Brasseur and Solomon*, 2005].

[26] Molecular oxygen (O_2) also figures into both day and night determinations of *O* and in the ozone photolysis rates. The molecular oxygen mixing ratio gradient is quite weak in the mesosphere and therefore we believe the contribution of its variation to the variability of atomic oxygen is minor compared with the other processes included. We set the O_2 mixing ratio to a constant value of 0.205. O_2 will be slightly overestimated in the upper mesosphere because of neglect of the small decrease in O_2 mixing ratio with altitude and therefore *O* will be slightly underestimated. There is at present no reliable determination of O_2. Using a numerical model, we have found that the assumption that $2 \times O + O_2$ is constant does not hold in the upper mesosphere because of redistribution by molecular diffusion.

[27] All the calculations are done on pressure levels. Before *O* is determined, the data products are interpolated from the irregular Level 2 grids to fixed pressure levels with a spacing of 0.3 in log pressure. The altitudes corresponding to each pressure level are averaged over all latitudes and yaw periods and given on the figures.

[28] Minimal screening of the temperature profiles is used to eliminate those profiles with negative temperatures (a signal of missing data) and to discard profiles in which the pressure levels are not sequential. The ozone and *OH* emission data are then screened using the method described by *Smith et al.* [2008]. In brief, we sort all of the available data at each pressure level into bins depending on the retrieved value. Profiles with any values that fall into the top 0.1% are discarded. This screening retains most values; *Smith et al.* [2008] showed that the large nighttime ozone values remaining after screening fit nicely with theory. No additional screening is applied to the retrieved profiles of *O*.

[29] From (10), it is evident that there could be problems with the solution if the loss of ozone by reaction with atomic oxygen is as large as or greater than the production rate of ozone, in which case the denominator in the right side of the equation is zero or negative. This would be an indication that either ozone is not in equilibrium or that there are data errors. In the results presented here, we test for the ratio of the atomic oxygen destruction term (1c) to the production term (1a). This ratio is $(k_3 \cdot [O_3])/(k_1 \cdot [O_2] \cdot n)$. No atomic oxygen retrieval is done where the ratio exceeds 0.33. This almost never occurs below 85 km but becomes a factor above ~0.002 hPa (87 km). At ~0.0004 hPa (98 km), about 20% of the cases are not retrieved. The omitted retrievals are scattered globally and during all months although they are most common at high latitudes. In general, they are associated with higher temperatures, where the ratio $k_3/(k_1 \cdot n)$ is higher.

[30] SABER retrievals of the volume emission rate of the 2.0 μm Meinel emission are available through the upper part of the middle atmosphere and into the lower thermosphere. The signal to noise at the altitude of the emission peak (87 km) is typically 600–800 so the measurement has excellent precision. The signal is weak outside of the range 70–105 km altitude. However, this is not the only constraint affecting the top and bottom cutoff for performing the *O* retrievals. The cutoff is determined by the breakdown in the assumption that nighttime ozone is in photochemical equilibrium. In the results that follow, we have presented retrieved results down to 0.01 hPa, approximately 80 km. According to our model calculations using the same chemical formulation and rate coefficients as in the SABER *O* retrievals, the equilibrium assumption is valid in the mesosphere above 0.01 hPa except close to dawn and dusk when the composition is changing rapidly. The upper cutoff due to the breakdown in photochemical equilibrium is ~0.0002 hPa, about 103 km. Nighttime profiles with a solar zenith angle less than 110° are not retrieved.

[31] The 2.0 μm Meinel emission is measured by SABER during both day and night. We do not use it for the daytime *O* retrieval because the ozone loss by reaction (1b) is very minor compared to that by reaction (1d) during daylight. It would therefore not be possible to get a stable retrieval of daytime *O* using the 2.0 μm emission. Since there is a substantial change in the concentration of mesospheric ozone between day and night (much lower concentrations during the day), we would expect the emission to undergo a large shift at sunrise and sunset.

[32] The SABER atomic oxygen retrievals with the improved algorithm described in section 2.1 have not been processed as an operational product as of this writing (February 2010). The retrieval used in this paper is similar but has some differences from the proposed operational retrieval. (1) All data are interpolated to a fixed pressure grid before the calculation whereas the operational retrieval will process data at the more closely spaced pressures/altitudes available from Level 1 data. (2) The ozone photolysis rate

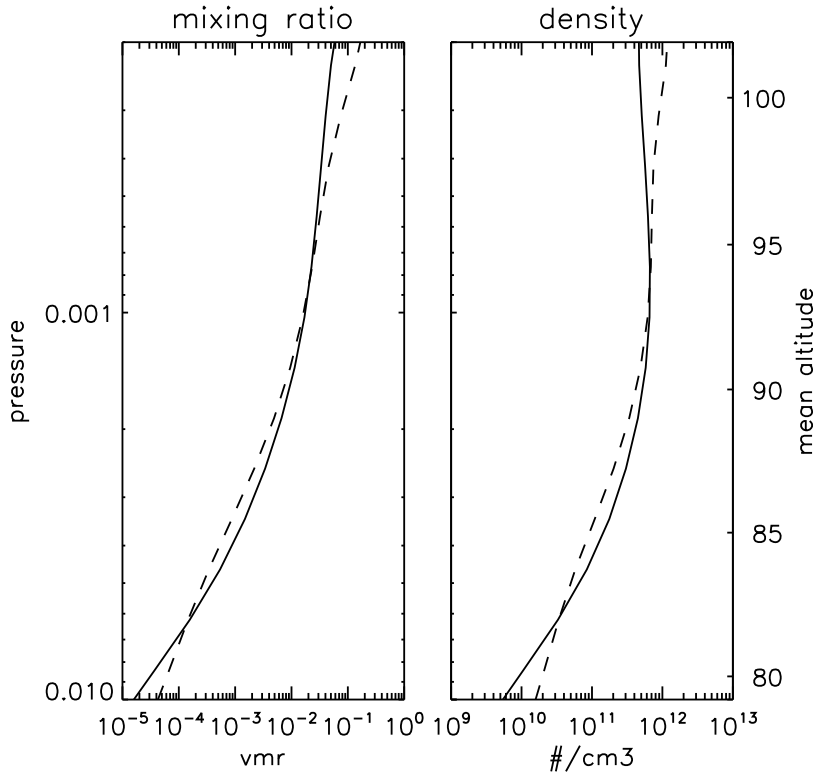

Figure 2. Profiles of global mean atomic oxygen averaged over all latitudes for 7.6 years. Solid is nighttime; dashed is daytime. Units are (left) volume mixing ratio and (right) number density (cm^{-3}).

calculation (the TUV model) is different; the operational algorithm obtains photolysis rates as a product of the daytime ozone retrieval. (3) The ozone loss rate due to reaction with atomic oxygen (1c) is included here (see equation (10)) but is not currently implemented in the operational algorithm. (4) The current analysis does not retrieve data if the SABER day/night flag indicates twilight or if the flag indicates night but the solar zenith angle is less than 110°.

3. Mean Day and Night Atomic Oxygen

[33] A validation of the absolute values of *O* is difficult because there are not many other observations for comparison. The other observations are subject to the same or similar uncertainties that we encounter in the SABER *O* retrieval. One advantage in this analysis is the possibility of using consistency between the day and night retrieved values as a check.

3.1. Mean Profiles

[34] *Llewellyn and McDade* [1996], *Mlynczak et al.* [1998] and *Russell and Lowe* [2003] have pointed out the uncertainties in the Einstein coefficients, the quenching rates, etc. that go into the determination of nighttime *O* from the hydroxyl airglow emission. There are few laboratory measurements and the differences between measurements can be substantial. In this paper, we use the values for these parameters that are accepted by consensus of the SABER team (Table 1) and are expected to be used in the upcoming standard SABER processing algorithm.

[35] Figure 2 shows profiles of the global mean volume mixing ratio and number density during day and night. Results at selected pressure levels are given in Table 3. Standard deviations of the day and night volume mixing ratio are also given in the table. Daytime values are larger than nighttime values at 0.01 hPa, as expected from photochemical theory.

Table 3. Daytime and Nighttime Density, Volume Mixing Ratio, and Standard Deviation of Volume Mixing Ratio for Atomic Oxygen at Selected Pressure Levels[a]

	Pressure			
	0.01 hPa	0.003 hPa	0.001 hPa	0.004 hPa
Mean altitude (km)	79.2	86.2	92.7	97.9
Day O density (cm^{-3})	1.58 e+10	1.43 e+11	6.22 e+11	7.66 e+11
Night O density (cm^{-3})	5.44 e+09	2.23 e+11	6.56 e+11	5.58 e+11
Day O vmr	4.61 e-05	1.44 e-03	1.65 e-02	5.01 e-02
Night O vmr	2.06 e-05	2.32 e-03	1.75 e-02	3.46 e-02
Day standard dev	3.57 e-05	1.11 e-03	8.99 e-03	4.35 e-02
Night standard dev	3.62 e-05	2.12 e-03	9.28 e-03	4.30 e-02

[a]Data are based on averages over 7.6 years.

Atomic oxygen has a short lifetime there and so its concentration increases during the day as a result of photodissociation of O_2. Above about 82 km, there are differences between the day and night values but they are small until altitudes near the mesopause (0.0004 hPa, ~98 km). At these upper levels, O is again higher during day than night. The observed signals for the emissions used to determine O from the Meinel bands and from daytime ozone are weak here. In addition, the number of cases where there is no solution due to a large value of ozone loss by (1c) increases above 0.001 hPa. We do not know whether the low signal or the increasing importance of reaction (1c) is responsible for the differences but data at pressures lower than 0.0004 hPa are not considered further in this paper.

[36] As the duration of the SABER data record increases, the proportion of the data that were obtained during a state of low solar activity has increased and the atomic oxygen averaged over the mission has decreased. Even accounting for this decrease, the SABER nighttime O is appreciably higher than that derived by *Russell et al.* [2005] from data collected by the Wind Imaging Interferometer (WINDII) satellite instrument. From SABER, the mixing ratio reaches 10^{-3} around 85 km and reaches 10^{-2} around 90–92 km. The WINDII results show vmr of 10^{-3} at about 87 km and vmr of 10^{-2} around 95 km. These translate into a vmr difference of a factor of 3–5; SABER O is larger. The O derived by *Russell et al.* [2005] included values determined from the hydroxyl nightglow as well as from the oxygen greenline emission. The hydroxyl transition used (8–3) [see *Russell and Lowe*, 2003] was different than the (9–7) and (8–6) transitions used in the SABER retrieval. *Russell and Lowe* [2003] found good comparison of the hydroxyl results with O determined from the greenline emissions, providing support for the values they calculated. Recall that the SABER 2.0 μm channel was chosen because the number of parameters involved in modeling the emission is smaller when the vibrational levels are populated directly by reaction (1b) rather than by cascade downward. The SABER model used to relate the emission to the physical state of the atmosphere is therefore simpler and more direct.

[37] SABER O densities (see Figure 2) are also larger than those from the reference model compiled by *Llewellyn and McDade* [1996]. Their monthly and latitudinal mean values never exceed 4.6×10^{11} cm^{-3} whereas the SABER annual global mean density peak is 7×10^{11} cm^{-3}. The mean O retrieved from SABER is larger than that from the NRL-MSIS00 empirical model [*Picone et al.*, 2002] but the agreement is closer than with the other data sets mentioned here. The SABER diurnally averaged O is larger than the NRL-MSIS00 values by about a factor of two. *Gattinger et al.* [2010] retrieved O densities from a limited amount of Odin-OSIRIS data (covering the Southern Hemisphere over 24 h). They also found that the O densities were larger than those from the NRL-MSIS00 empirical model at altitudes below about 98 km.

[38] The Meinel band quenching rates are not the only uncertainties in the retrieval. Another parameter that affects the SABER nighttime O retrieval is the reaction rate k_2. The uncertainty at mesospheric temperatures can be large (a factor of two at 175 K and greater uncertainty for colder temperatures [*Sander et al.*, 2006]).

[39] As demonstrated below, the nighttime and daytime values of O are quite consistent. If the nighttime O were reduced fourfold to bring it into line with the O retrieved by *Russell et al.* [2005], this would no longer be the case. To have day/night agreement and also lower nighttime O, the daytime O would need to be lower as well. The daytime and nighttime retrievals share some factors since both depend on reaction (1a). An error in one of these shared factors (k_1, [O_2], n) would affect day and night values in a similar way and would maintain consistency. k_1 has an uncertainty estimate of a factor of 1.4 at 175 K [*Sander et al.*, 2006] so it alone would not account for a twofold or fourfold error in O. An error in the SABER temperature would also affect the O during both day and night but would not affect them equally. A large increase in T (e.g., from 190K to 233K) would be required to decrease $k_1 \cdot n$ by a factor of 2. Such a T increase would simultaneously increase k_2 and k_3 and disrupt the day/night agreement. At this point, we have no reason for believing that there are substantial systematic errors in any of the SABER measurements that go into determining these fields or in the laboratory-determined magnitude or temperature dependence of the kinetic rate coefficients.

[40] One final aspect of the retrieval that contributes to the higher O found in the SABER nighttime retrievals is the inclusion of reaction (1c). It has not been possible to consider this in previous analyses because of the lack of reliable nighttime O_3 measurements in the upper mesosphere. Equation (10) shows that inclusion of this reaction increases the retrieved O.

3.2. Test for Self-Consistency Between Day and Night

[41] To provide support for the O retrieval and for the selection of parameters used, we look for consistency between the atomic oxygen during day, which is not as strongly affected by these uncertainties, and that at night.

[42] In general, the time-dependent behavior of O is given by

$$\frac{dO}{dt} = P - L \cdot O, \tag{11}$$

where now O represents the volume mixing ratio ($O = [O]/n$) rather than number density. P is production, L is the loss rate, and d/dt is the material derivative, including advective transport and diffusive mixing. Above 85 km, where the lifetime of atomic oxygen is weeks to months, we can assume that diurnal variations in O are caused by transport, not photochemical production and loss, and therefore on this time scale $dO/dt \approx 0$. Because the vertical gradient of O can be quite large, we focus on the vertical transport. The migrating diurnal tide is a source for regular vertical winds. We look at the equatorial region where horizontal winds of this tide are small and vertical winds are at their largest. Because of the very strong vertical gradients of O, the changes in concentration due to transport by the tidal vertical wind can be quite large. In the expression that follows, we neglect transport by horizontal tidal winds and by the time mean meridional and vertical winds.

[43] All fields can be separated into time mean (overbar) and tidally varying (prime) parts.

$$\left(\frac{\partial}{\partial t} + \bar{u}\frac{\partial}{\partial x}\right)O' + \frac{\partial \overline{O}}{\partial z}w' = 0 \tag{12}$$

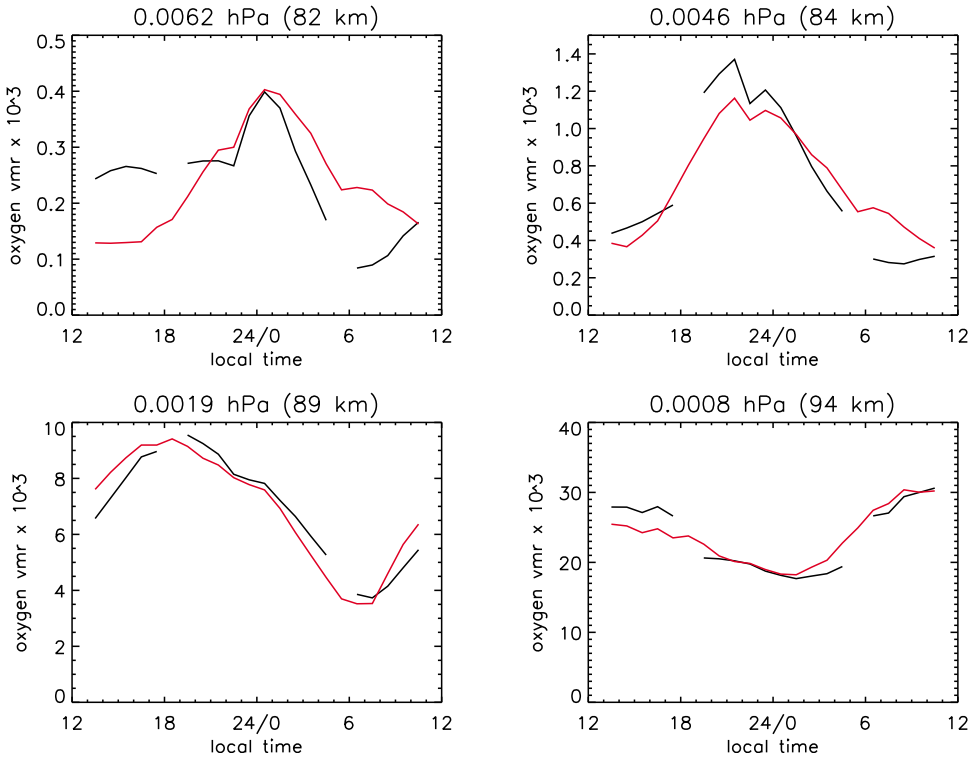

Figure 3. Local time variation of atomic oxygen at specified pressure levels derived from SABER emissions (black) and predicted using the assumption that variations are due to vertical transport (red) averaged over the latitudes 20°S–20°N. Units are volume mixing ratio $\times 10^3$.

$\bar{u}$ is the zonal mean zonal wind and w' is the vertical velocity of the tide. Assuming tidal variations of the form $\exp[i(kx - \sigma t)]$, where k is the zonal wave number and σ is the tidal frequency, gives

$$i(k\bar{u} - \sigma)O' + \frac{\partial \overline{O}}{\partial z} w' = 0. \tag{13}$$

A similar expression can be written for the tidal temperature variations, neglecting diabatic terms

$$i(k\bar{u} - \sigma)T' + S \cdot w' = 0, \tag{14}$$

where S is static stability $S = (\partial T/\partial z + g/c_p)$, g is the acceleration of gravity, and c_p is the heat capacity at constant pressure. These combine to give a relationship between perturbations in O and T

$$O' = \frac{\overline{O}_z}{S} T'. \tag{15}$$

[44] To check for consistency, we focus on the low latitudes where diurnal variations are large due to the large amplitude of the vertical velocity from the diurnal tide. Atomic oxygen and temperature values for each yaw cycle over all years are combined into bins of 1 h using all profiles between the latitudes 20°S to 20°N. The zonal and time mean profiles of O and T, which are needed to determine the vertical gradients, are calculated from the hourly bins. The predicted atomic oxygen, including variations due to tidal transport, is

$$O_{predicted} = \overline{O} + \frac{\overline{O}_z}{S} T'. \tag{16}$$

Figure 3 shows the SABER derived atomic oxygen along with the prediction. Figure 3 uses observations from 8 years (2002–2009) but only for the yaw period covering vernal equinox (approximately days 75–140 of each year), which is when the SABER diurnal tide in temperature is largest [*Xu et al.*, 2009]. Other periods show similar agreement but the variations have smaller amplitudes. As expected, the prediction based only on vertical transport does not agree with the observations below 82 km, where the lifetime of O is short. At these levels, O has a daytime maximum due to photolysis of O_2. However, above 84 km, the agreement is excellent despite of the assumptions inherent in (12).

[45] The sampling due to orbit precession requires about 60 days to cover the full range of local time. The pattern at the equator is such that sampling begins around noon or midnight and then moves backward in local time through dawn and dusk, respectively, to local times roughly 12 hours earlier. On the local time plots, there can be a discontinuity at noon/midnight since measurements on either side are separated by about two months. The apparent tidal signal includes this longer-term seasonal change in the daily mean fields as well as the actual tide.

[46] Figure 3 does not demonstrate that the O values are correct, only that the diurnal variations are consistent with

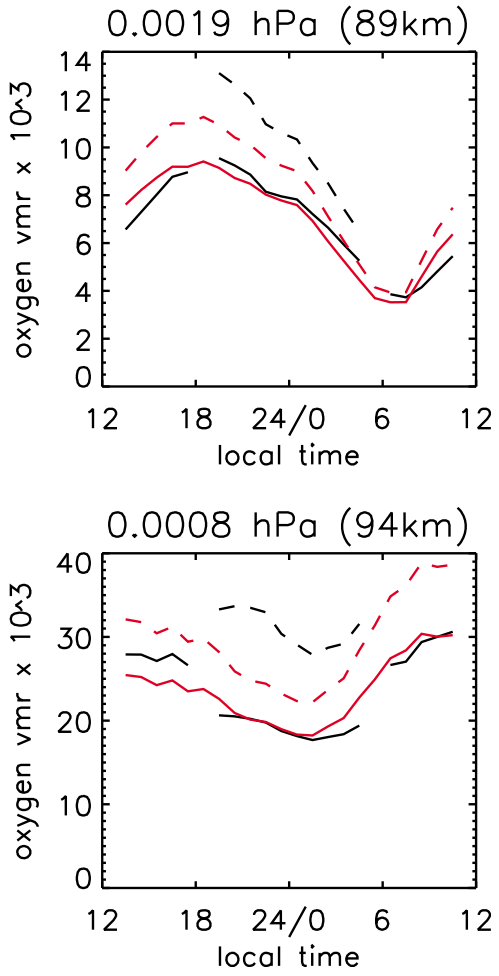

Figure 4. Local time variation of atomic oxygen at specified pressure levels derived from SABER emissions (black) and predicted using the assumption that variations are due to vertical transport (red). In the night retrievals, the solid lines use $k_9^O = k_8^O = 5 \times 10^{-11}$ and the dashed lines use $k_9^O = k_8^O = 2 \times 10^{-10}$. Units are volume mixing ratio $\times 10^3$.

vertical transport by the diurnal tide. It is shown here to demonstrate that there is a high degree of consistency between the retrievals during day and night. For comparison, Figure 4 repeats the results at 0.0019 and 0.0008 hPa but also includes the analysis using higher values of k_9^O and k_8^O, the quenching of vibrationally excited $OH(v = 9)$ and $OH(v = 8)$ by O. With stronger quenching rates, the retrieved daytime values are identical (since the OH emission does not factor into the daytime retrieval) but the night O is much higher. The resulting "predicted" O variation (dashed red line) falls between the day and night values but does not agree well with either. The excellent day/night agreement that had been found when using $k_9^O = 5 \times 10^{-11}$ and $k_8^O = 5 \times 10^{-11}$ is lost when we instead use $k_9^O = 2 \times 10^{-10}$ and $k_8^O = 2 \times 10^{-10}$. The day/night comparison in Figure 4 gives support for the choice of the values for k_9^O and k_8^O used in the retrieval. Smaller values of these quenching parameters (not shown) have a much smaller impact on the retrieved O.

[47] Figure 5 shows the averaged O mixing ratio as a function of latitude and pressure for day and night, averaged from 25 January 2002 to 15 September 2009 (46 yaw periods, about 7.6 years). In order to give equal weighting to each local time and season, the data are first sorted into local time and latitude bins and then averaged for each yaw period. Latitude bins are 10° and local time bins are 1 h. The atomic oxygen mixing ratio varies by 5 orders of magnitude in the upper mesosphere. The variation is strong and monotonic in pressure. Data poleward of 55° are available only in alternate yaw periods. There could be a bias in the high-latitude averages due to the repeating seasonal pattern in coverage, which always extends toward the summer pole during solstices (Table 2). There are more high-latitude data for the summer months than for the winter months. The latitudinal variation in Figure 5, which shows that atomic oxygen is lower at high latitudes through most of the range shown, could be at least in part a result of the sampling bias toward the summer solstice.

[48] Figure 5 also shows the ratio of night to day atomic oxygen mixing ratio over the latitude range having both day and night coverage within individual yaw periods. The strong tidal signal is clearly evident at all latitudes. The diurnal tide perturbation is characterized by a 24 h oscillation that has maximum amplitude at the equator, perturbations of opposite sign around 30° of both hemispheres, and a vertical wavelength of about 25 km. In the lower levels where O has a shorter photochemical time scale, day concentrations always exceed those at night. Even there, latitudinal variation in the night to day ratio associated with the tide is clearly evident.

[49] There have been reports of large variations of atomic oxygen that did not appear to be associated with the regular cyclic pattern due to the migrating tides [e.g., *Shepherd et al.*, 1993; *Hecht et al.*, 2004]. Very large amplitude perturbations could affect the average concentrations in some local time × latitude bins and therefore have an erroneous impact on the deduced diurnal cycle or on longer period (seasonal or interannual) variations. The regular sinusoidal variations seen in Figure 3 suggest that this is probably not a major factor. Individual years show a pattern very much like the multiyear average although the amplitudes vary from year to year. If the retrieved O is strongly affected by noise in the input fields, then averaging the input first would alter the resulting retrieved values. To test this, we altered the order of the computation by first binning and averaging the temperature, OH volume emission rate, and ozone in local time and latitude for each yaw period and then using these averaged fields to compute the O. This did not have any appreciable impact on the mean values or the diurnal and seasonal cycles of the results.

[50] The profile averaging was done to address the scientific goals of this study. Because of the good precision of SABER measurements of the mesospheric fields that go into the atomic oxygen retrieval (OH volume emission rate, temperature, ozone), individual profiles have high information content and could be used to address questions of intermittent variability.

4. Variation of *O* in the Upper Mesosphere

[51] Now that consistency between day and night atomic oxygen in the upper mesosphere has been demonstrated, we present the results for the O variations.

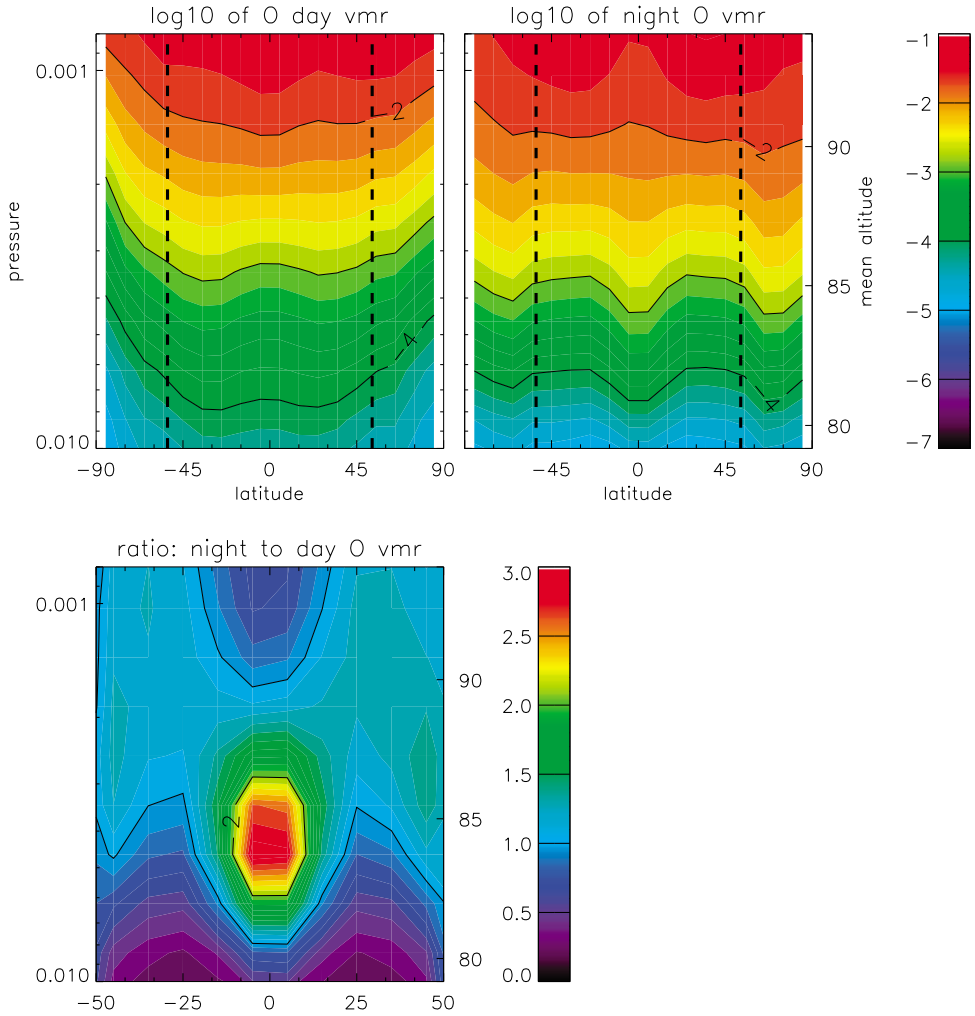

Figure 5. Latitude × pressure cross section of mean atomic oxygen averaged over 7.6 years for day and night (units are $\log_{10}$ of volume mixing ratio) and the ratio of night to day atomic oxygen vmr for low and middle latitudes. The thick dashed lines at 53°N and S separate high-latitude regions sampled on alternate yaw periods from lower latitudes with continuous sampling.

4.1. Local Time Variations

[52] Figure 6 shows atomic oxygen averaged over 7.6 years as a function of local time and latitude at four pressure levels. Results are not plotted if there are data for only one of the seven or eight yaw periods for any season. Local time bins around dawn, noon, and dusk have poorer coverage. *O* for the hourly bins of 5–6 h and 18–19 h do not vary smoothly, probably because of substantially fewer profiles due to the omission of twilight and dawn/dusk data. As noted above, there is a gap in the data around noon due to the SABER sampling.

[53] The atomic oxygen variation in local time near the equator is approximately sinusoidal with a wave number one. There is little diurnal variation near ±20° and then the wave number one pattern reappears but with the opposite phase at ±30°. The wave number 1 pattern in local time is not as well defined at ±30°. The phase of the equatorial perturbation shifts with altitude and has a vertical wavelength of about 25 km.

[54] The signature of the diurnal migrating tide can be identified by the local time and latitude structure. This is characterized by a sinusoid in local time and a distinctive (1,1) Hough mode latitudinal structure having maximum amplitude at the equator flanked by weaker maxima of opposite sign at ±30°. The structure of the diurnal tide is clearly evident in all levels in Figure 6, particularly during night. Diurnal tidal signals in *O* should resemble those in temperature (15). This is indeed the case, as confirmed by comparison with temperatures at the same levels (Figure 7). At all levels, the tidal signal is most evident at night. For example, during the morning (6–12 h) at 0.0019 hPa and during the afternoon (12–18 h) at 0.0008 hPa, there is not a clear tidal signal in either *T* or *O*.

[55] At all levels in the tropical upper mesosphere, the atomic oxygen variation during night looks similar to the diurnal tide in temperature. Specifically, there is a strong maximum or minimum in a narrow band near the equator and perturbations of the opposite sign in the subtropical

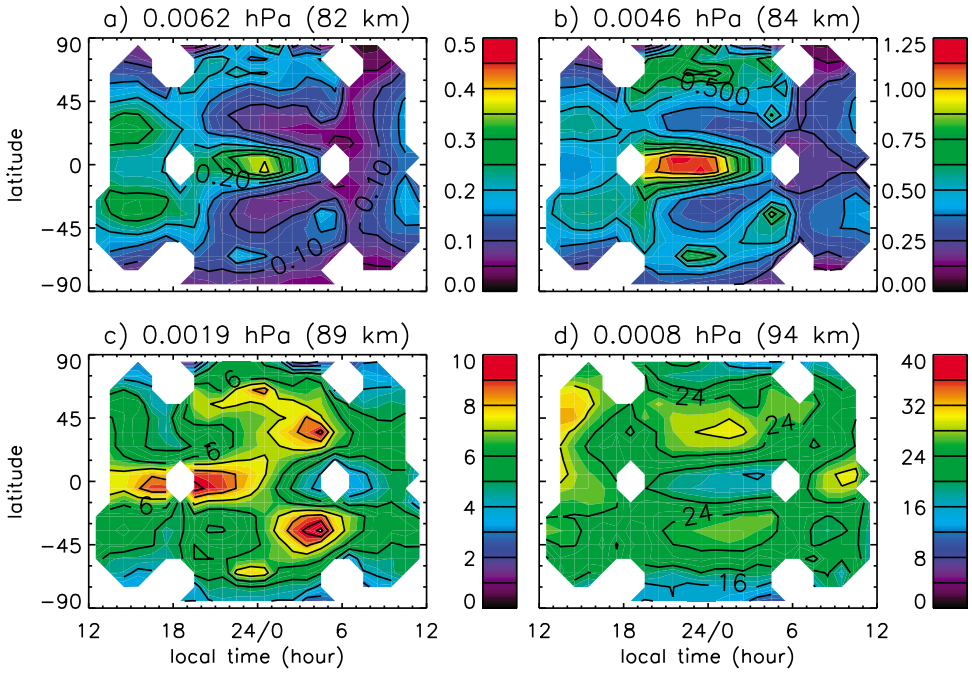

Figure 6. Local time variation of atomic oxygen at all latitudes at four pressure levels averaged over 7.6 years. Units are volume mixing ratio $\times 10^3$.

latitudes. At all levels the *O* also has a more complex structure (less characteristic of the migrating diurnal tide) during daytime. The patterns in day and night temperature are similar, indicating that the cause is not an error in the radiances from 9.6 μm or 2.0 μm that are used to retrieve *O* but are not used in the temperature retrieval. Because of the large volume of data over 7.6 years, it is not likely that the daytime latitude/local time structure is due to a specific dynamical event. A survey of similar plots for each of the 46 yaw periods covered in this analysis showed that a similar reduction or disappearance of the typical Hough mode diurnal pattern was a feature in more than half of these periods. The reduced or missing Hough mode pattern occurred for all periods that included one of the equinoxes

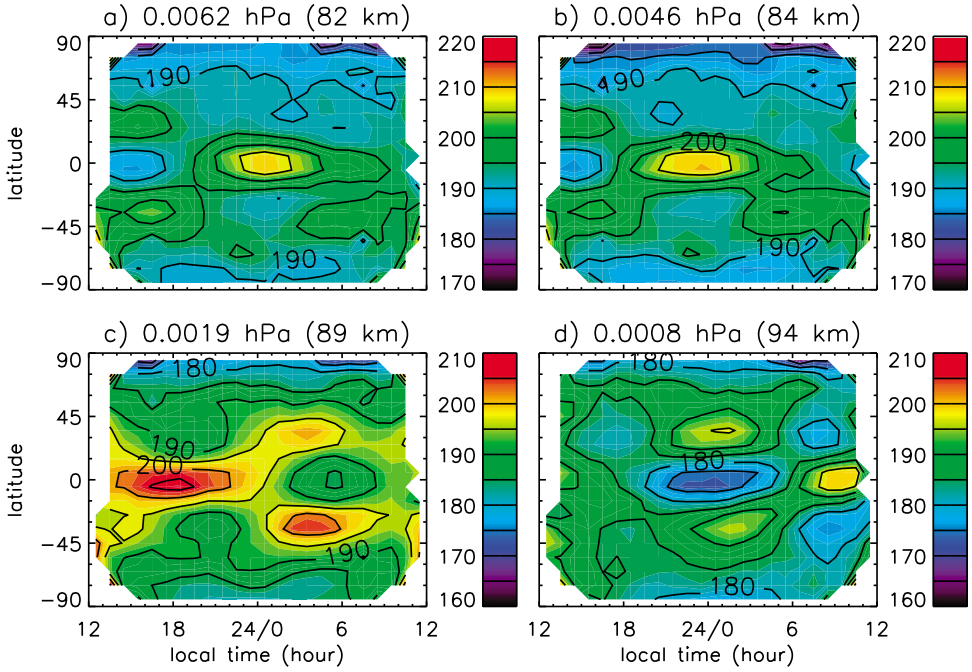

Figure 7. Local time variation of temperature at all latitudes at four pressure levels averaged over 7.6 years. Units are K.

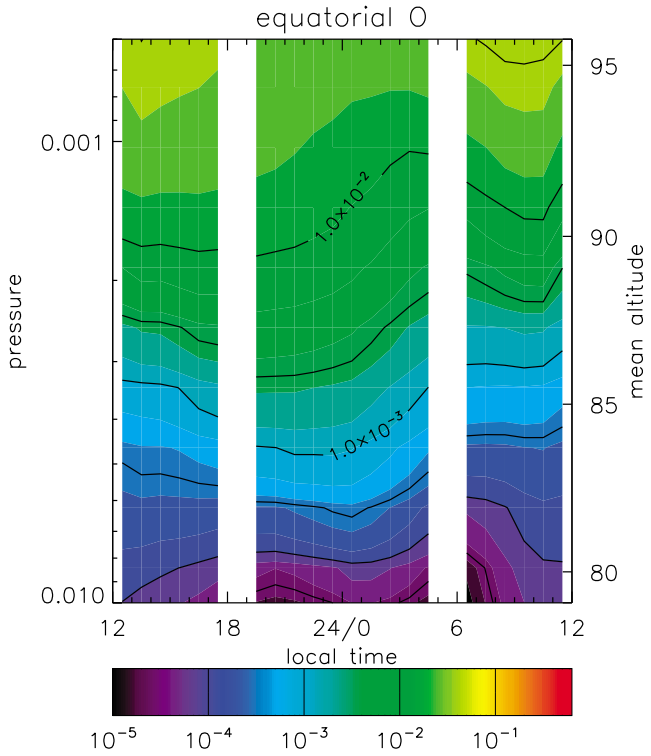

Figure 8. Local time variation of atomic oxygen averaged over latitudes 10°S to 10°N for 7.6 years. Units are $\log_{10}$ of volume mixing ratio.

(the yaw periods from mid-March through mid-May and from mid-September through mid-November) when the migrating diurnal tide amplitude was large. The daily variation of meridional winds from HRDI at 95 km [*Burrage et al.*, 1995] also showed a less well defined structure for these same local times.

[56] The local time binning used to make Figures 6 and 7 does not filter the variations to isolate the diurnal tide. Although nonmigrating modes are excluded by the processing, the variations can include contributions from other migrating tidal frequencies (semidiurnal, terdiurnal, etc.) in addition to diurnal. *Pancheva et al.* [2009] show that the amplitude of the migrating semidiurnal tide in SABER temperature is small at the equator but can be large in the subtropics and midlatitudes. The maximum monthly average amplitude at 95 km is about 6K. Superposition of the diurnal and semidiurnal tides will have little impact on the diurnal tidal signal at the equator but can distort or mask the apparent diurnal signal away from the equator. For example, the semidiurnal temperature phases at 20°N and 90–95 km [*Pancheva et al.*, 2009] are variable but are frequently near midnight. The semidiurnal phase at 20°S tends to be shifted toward later times relative to that at 20°N. Accounting for these semidiurnal signals can explain the temperature perturbations north and south of the equator in Figures 7c and 7d and, by analogy, in Figures 6c and 6d.

[57] Although the day and night *O* profiles are determined from independent techniques, both rely on (1a). The rate coefficient (k_1) is strongly temperature dependent. From (3), we see that the derived daytime *O* depends on the inverse of k_1. At night (10), neglecting the contribution from reaction (1c), the derived *O* also depends on the inverse of k_1. The sign is such that an increase in temperature will give an increase in the retrieved atomic oxygen. This brings up the question of whether the tidal signal in *O* and its agreement with that in *T* result from this built-in aspect of the *O* retrievals or whether the signals of *OH VER* (used at night) and ozone (used during the day) also show the same pattern. As a test on this, we repeated the calculation of *O* except that the temperature in rate coefficient k_1 was replaced by the global mean temperature for that particular pressure level. All other temperatures used in the retrievals were normal. The tidal signals are of course smaller in this case but have an identical structure to that shown in Figure 6. Additional evidence showing that the tidal signal is a prominent feature of the *OH VER* variability was presented by *Marsh et al.* [2006].

[58] The local time variations as a function of pressure averaged over 10°S to 10°N (Figure 8) also illustrates the large impact of the diurnal tide on *O*. Here the $\log_{10}$ of the *O* vmr is shown so that patterns can be identified over a wide vertical range. As expected from Figure 3, the atomic oxygen varies in a sinusoidal fashion with an hour of maximum that moves downward with time.

4.2. Seasonal and Longer-Term Variations

[59] Atomic oxygen mixing ratios averaged over each calendar day for the 7.6 years at 0.0046 hPa (~84 km) are shown in Figure 9a. The smoothness of the variations illustrates the high precision of the SABER measurements. At latitudes poleward of 55°S or 55°N, data are available only every other yaw period. Atomic oxygen variations are dominated by semiannual equinoctial maxima near the equator and annual wintertime maxima in high latitudes of both hemispheres. Figure 9b shows latitude × time variations of the yaw period mean *O* mixing ratio at the same level. Because of the TIMED orbit precession, this mean is approximately the mean over 24 h of local time.

[60] The equatorial maxima in *O* have the appearance of a semiannual oscillation (SAO) confined to low latitudes, which invites comparison with the SAO of the mesospheric zonal mean wind [*Garcia et al.*, 1997]. A semiannual circulation driven by waves would produce SAO patterns in temperature and trace species that have strong gradients and long enough lifetimes. *Buriti et al.* [2004] suggested that the SAO contributed to the semiannual variation in the intensities of several airglow bands that they observed near the equator. We do not believe that this is an important mechanism for the atomic oxygen variations at 0.0046 hPa. The SAO in SABER temperature (not shown) is very weak. In addition, the lifetime of atomic oxygen at this level, while long compared to a day, is not long enough for it to be conserved over a cycle of the SAO.

[61] A more likely source of the SAO in atomic oxygen is the large semiannual variation in the amplitude of the migrating diurnal tide. The vertical gradient of *O* at 84 km is steep, especially during night (Figures 5 and 8), and there is significant tidal transport. Downward motion by the tide brings down air that is rich in *O*, creating a maximum in the equatorial region. Away from the tropics or during times when the tidal amplitude is smaller, tidal transport is less vigorous or is absent altogether so the atomic

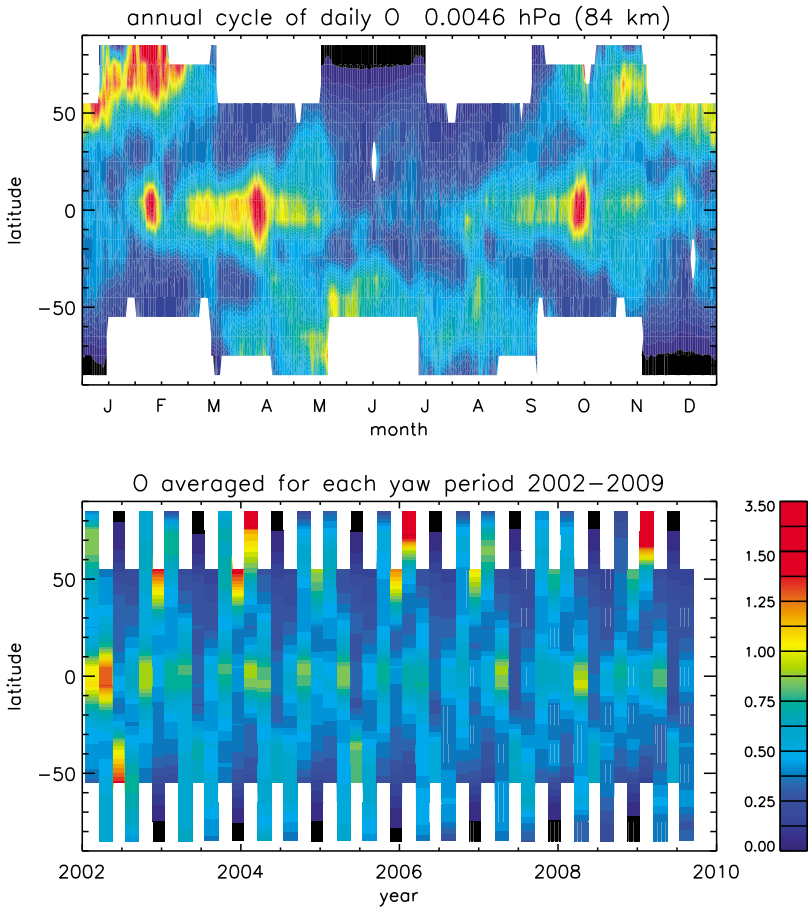

Figure 9. (top) Latitude and annual variation of averaged daily atomic oxygen at 0.0046 hPa. (bottom) Atomic oxygen at 0.0046 hPa averaged for each yaw period. Units are volume mixing ratio $\times 10^3$.

oxygen amount relaxes more rapidly toward the (smaller) photochemical equilibrium mixing ratio. At the other phase of the tide, separated by ~12 h, transport is in the other direction (average upward).

[62] By this argument, if transport of *O* by tidal motions were completely reversible, there would be no tidal signal in the yaw-period average fields shown in Figure 9. The existence of an apparent tidal signal in these averages indicates that there is a net transport. There are two basic mechanisms that contribute to irreversible transport. First, where there is a strong gradient in photochemical lifetime in a region where the lifetime is similar to the transport time (~1 day for the diurnal tide), then there will be a net transport from areas with the longer lifetime to those with the shorter. This mechanism is known as chemical eddy transport [*Smith et al.*, 2003]; it acts even when there is no net transport of air parcels over the period of the wave. Transport of *O* by the diurnal tide is important near 84 km because of the sharp gradient in the *O* chemical lifetime there and because the lifetimes are short. It is expected to have a much weaker impact near the tropical mesopause where the *O* lifetime is consistently long. The second mechanism is actual transport of air parcels. A dissipating tide will generate Eliassen-Palm (EP) flux divergences which generates a circulation to maintain conservation of potential vorticity [*McLandress et al.*, 2006]. The net motion from that circulation will lead to transport of *O* as long as its mixing ratio has a vertical gradient. This process is more important near the mesopause because of the dissipation of the diurnal tide there. Both processes will vary in time as the amplitude of the tide varies. For example, *McLandress et al.* [2006] presented EP flux divergence from a model calculation that showed strong semiannual variation in the equatorial upper mesosphere due to interaction with the diurnal tide.

[63] Figure 10 shows the *O* variation near the equator at two levels separated into day and night. At 84 km, the vertical motion of the diurnal tide gives a maximum of *O* at night while at 94 km, the local time variation gives the maximum during day (see also Figures 5 and 6). In both cases, there is a strong semiannual cycle with equinoctial peaks during the local time period of the *O* maximum. At the other times (day at 84 km; night at 94 km), the seasonal variation is much smaller and there is not a clear semiannual cycle. Figure 10 suggests that the net transport at both levels is in phase with the downward transport, whether that is during day (94 km) or night (84 km). As discussed above, the mechanism leading to net transport may be different in these two altitude levels. At 80–85 km, where there is a very strong gradient in *O* lifetime, chemical eddy transport is likely to be a major contributor. Above 90 km, the chemical

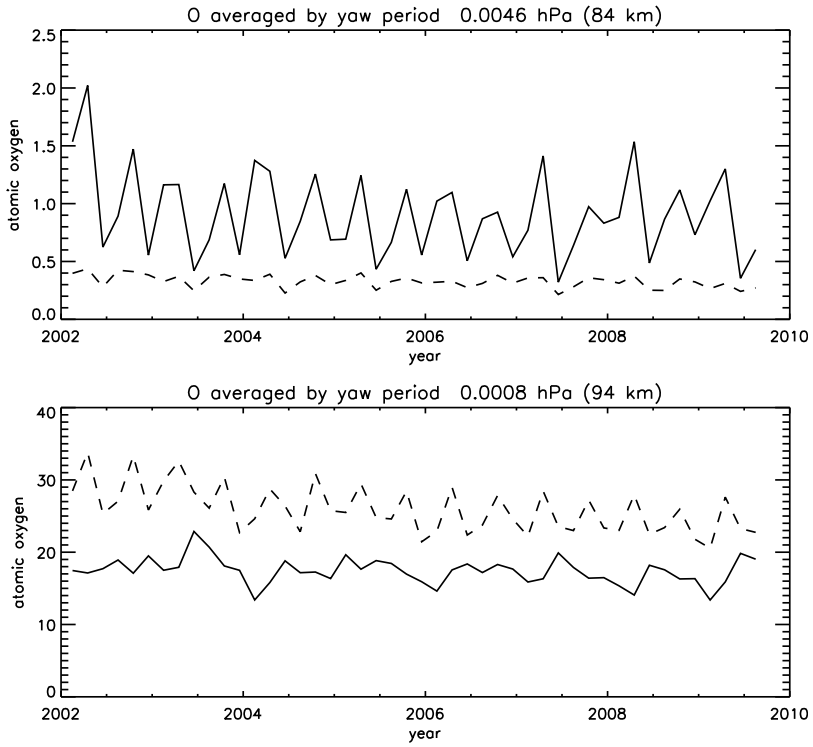

Figure 10. Variation of atomic oxygen at 0.0046 and 0.0008 hPa averaged for each yaw period over the latitude band 10°S to 10°N. The dashed line includes daytime only, and the solid line includes nighttime only. Units are volume mixing ratio $\times 10^3$.

time scale is long but a circulation driven by tidal dissipation could account for the transport.

[64] It appears from Figure 10 that the ratio of equatorial day to night *O* is declining over the period of the observations but the apparent trend in this ratio is not statistically significant.

[65] At high latitudes (Figure 9), the *O* mixing ratio at 84 km has wintertime maxima that are likely associated with the gravity wave driven downwelling circulation in the winter. The atomic oxygen in the NH is particularly high during the mid-January to mid-March yaw periods of 2004, 2006, and 2009. There is abundant evidence that the circulation and middle atmosphere structure were unusual during the later part of these winters [*Manney et al.*, 2005, 2008, 2009; *Siskind et al.*, 2007]. The unusual structure was associated with enhanced downward transport of *NO* [*Randall et al.*, 2005, 2006, 2009], NO_2 [*Hauchecorne et al.*, 2007], *CO* [*Jin et al.*, 2005; *Funke et al.*, 2009], and ozone [*Smith et al.*, 2009] as well as enhanced 2.0 μm OH Meinel emission [*Winick et al.*, 2009]. The enhanced atomic oxygen seen in Figure 9 is entirely consistent with the other trace gases that also have thermospheric origins and with the enhanced Meinel emission.

[66] *Manney et al.* [2005, 2008, 2009] give descriptions of the dynamical evolution during late January and February of these three winters. The location of the temperature maximum that defines the stratopause was not in its climatological position around 0.7 hPa (~50 km) but instead was as high as 80 km. The unusual thermal structure appears to have been caused by dynamical perturbations that occurred in the recovery stage of sudden stratospheric warmings. In these anomalous periods, planetary wave activity in the upper stratosphere was unusually low. Filtering by the anomalous stratospheric winds affected gravity wave penetration into the mesosphere. The unusual downwelling was likely related to the higher gravity wave activity in the mesosphere.

[67] At 0.0008 hPa, near the mean mesopause altitude, there is a marked decrease in the amount of *O* with time, especially at high latitudes (Figure 11b). A decrease was also seen by *Russell et al.* [2004] for the years 1992–1997. In the case of WINDII data analyzed by *Russell et al.* [2004], the relative change in *O* was larger in midlatitudes than at the equator. (WINDII data were not available at high latitudes.) The decrease may be due to the declining solar cycle; if so the trend will reverse as solar cycle 24 intensifies in the coming months and years. As the solar UV flux declines, there is reduced photolytic production of *O* and *H*, reduced temperature [*Marsh et al.*, 2007], and reduced magnitude of molecular diffusion. All of these could contribute to a solar cycle variation in *O*.

[68] Note that the phase of the midlatitude variation reverses between 84 and 94 km (Figures 9a and 11a). Maxima occur during winter near 84 km and during summer near 94 km. The level at which the shift occurs (not shown) is about 0.001 hPa (~93 km). *Russell et al.* [2004] found a similar reversal in the phase of the annual cycle in atomic oxygen density from WINDII at midlatitudes (±40°).

[69] The seasonal cycle at 94 km is predominantly an annual variation with maxima in summer at high latitudes. The gravity wave driven circulation is believed to be less

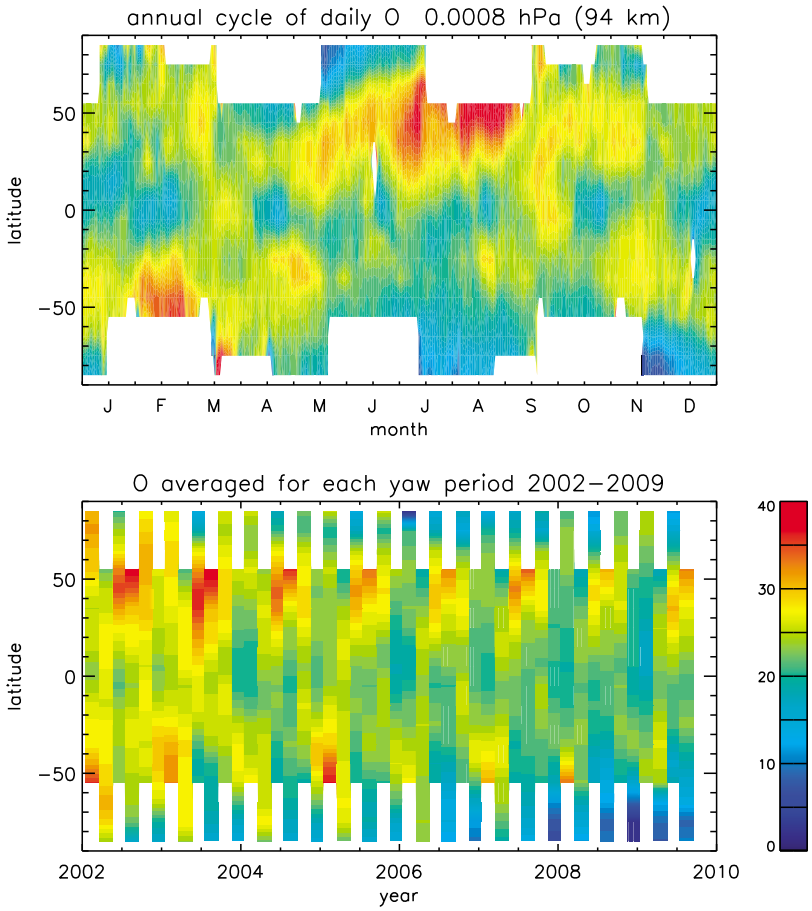

Figure 11. As in Figure 9 but for 0.0008 hPa.

vigorous at this altitude in the summer since many waves break near the mesopause, which is well below this altitude at the summer pole. The temperature is substantially warmer in the summer high latitudes than at the same pressures in low latitudes or in the winter hemisphere (not shown). Note that 94 km is below the mesopause altitude in the winter hemisphere, tropics, and low latitudes of the summer hemisphere. However, at summer high latitudes, the atmospheric structure is thermospheric in nature. The mesopause location during summer, as defined by the cold point in the temperature profile, is around 83–89 km [*von Zahn et al.*, 1996; *Xu et al.*, 2007]. The high summer atomic oxygen values could be an indication that the normal upwelling circulation seen in the summer mesosphere has reversed and there is a downwelling circulation cell. However, this cannot be verified from these data. Another possible cause is molecular diffusion, which would be enhanced with the high temperatures. Molecular diffusion mixes air with higher *O* down from the thermosphere and may contribute to the seasonal pattern seen in Figure 11.

5. Conclusions

[70] This paper presents the mean structure and temporal variability of atomic oxygen in the upper mesosphere derived from SABER measurements. Two different techniques are used to determine *O*; both are based on the assumption that O_3 is in photochemical equilibrium with *O*. During nighttime, emission by the Meinel bands from vibrationally excited hydroxyl gives the *O* amount. During daytime, enough information is available to determine *O* directly from the assumption of equilibrium with ozone.

[71] In the upper mesosphere, the lifetime of *O* is long and there should be no regular diurnal variation except that associated with transport by the atmospheric tides. To test the consistency of the day and night retrievals, we calculate the variation due to tidal transport (using the analogy between *O* and temperature) and compare this with the retrieved variation. The excellent agreement indicates that it is appropriate to combine results from these two retrievals to get the full diurnal variation of *O*.

[72] Atomic oxygen has a large diurnal variation at low latitudes associated with the diurnal tide. Atomic oxygen is in phase with temperature, indicating that vertical transport by tidal winds is responsible for the variation. The magnitude of the diurnal cycle in *O* can be as large as an order of magnitude. In the subtropics and midlatitudes, the local time variations in the upper mesosphere also include semidiurnal tidal signals.

[73] The seasonal variation of the daily mean *O* near the equator is also affected by the variations in diurnal tide amplitude. The seasonal cycle of *O* at any limited range of

local times (for example, nighttime only) near the equator will differ from that at other local times. Because of this, caution should be used in determining climatological *O* amounts or seasonal variations from any data with incomplete sampling in local time. The influence of the semiannual variation of the diurnal tide is clearly evident in the SABER equatorial *O* variation at the local times near the hours when the *O* is at its diurnal maximum. The variation is less apparent or even absent at local times when the *O* is at its diurnal minimum.

[74] This paper does not address the source of the mesospheric *O*. *O* is generated by the photolysis or breakdown of O_2. Because of the long lifetime of *O* in the MLT, the mesospheric *O* atoms could either be produced in situ or transported from another part of the atmosphere. The volume mixing ratio of *O* increases in the lower thermosphere so global mean mixing (diffusion) can increase the *O* concentration over what is locally produced [e.g., *Smith and Marsh*, 2005].

[75] The atomic oxygen amounts derived from SABER are higher by factors from 2 to 5 than those from other data sources [*Russell et al.*, 2005; *Llewellyn and McDade*, 1999], including the widely used NRL-MSIS empirical model [*Picone et al.*, 2002]. One contribution to the difference is the inclusion here, for the first time, of the reaction $O + O_3 \rightarrow O_2 + O_2$ in the formula for nighttime retrieval. The impact is an increase in the retrieved nighttime *O* above ~90 km. However, this addition does not fully explain the differences.

[76] The nighttime SABER retrieval uses a model of Meinel band emissions to link the observed emission to the reaction $H + O_3$, which produces vibrationally excited *OH*. The 2.0 μm emission measured by SABER is produced by vibrational transitions from v = 9 and v = 8, which are the highest levels that are populated by the reaction. Because of this, the model that is used to associate the observed emission with the *O* density in the SABER retrieval involves fewer transitions, and therefore fewer parameters, than retrievals using other Meinel emissions. Since each of the parameters has uncertainties, reduction in the number of parameters can help to reduce the overall uncertainty in the retrieval.

[77] Collisional quenching rates of excited vibrational states of *OH* are a major uncertainty for the nighttime retrieval. The *O* retrievals can provide constraints on some of these parameters. For example, the rate for the quenching of vibrational levels v = 8 and v = 9 by collision with *O* is uncertain. Using a rate higher than the one adapted gives *O* concentrations that are higher as well. A higher *O* concentration implies higher heating by the exothermic reaction $O + O + M \rightarrow O_2 + M$; the heating rate increases by the square of the *O* density. Concentrations of *O* that are substantially higher than those presented here would give heating rates in the MLT that are larger by an order of magnitude from those estimated in other data sets.

[78] While the main thrust of the current study has been to investigate variability in *O*, we also discuss the uncertainties in the retrieval. A piece of evidence supporting the SABER nighttime *O* values is the excellent agreement between the *O* mixing ratios retrieved at night and those determined independently for day. At this time, we do not have any reason for believing that the high *O* values from the SABER retrievals are incorrect. Further work is needed to narrow the uncertainties, resolve discrepancies with other measurements, and improve the quantitative determination of the middle atmosphere concentration of this key chemical constituent.

[79] **Acknowledgments.** The authors gratefully acknowledge the SABER science, algorithm, and data support teams. Support for this work was provided by the NASA Heliospheric Guest Investigator Program. The National Center for Atmospheric Research is sponsored by the National Science Foundation. Any opinions, findings, and conclusions or recommendations expressed in the publication are those of the authors and do not necessarily reflect the views of the National Science Foundation.

References

Adler-Golden, S. (1997), Kinetic parameters for OH nightglow modeling consistent with recent laboratory measurements, *J. Geophys. Res.*, *102*(A9), 19,969–19,976, doi:10.1029/97JA01622.

Brasseur, G. P., and S. Solomon (2005), *Aeronomy of the Middle Atmosphere*, 3rd ed., Springer, Dordrecht, Netherlands.

Buriti, R. A., H. Takahashi, D. Gobbi, A. F. de Medeiros, A. A. Nepomuceno, and L. M. Lima (2004), Semiannual oscillations of the mesospheric airglow at 7.4°S during the PSMOS observation period of 1998–2001, *J. Atmos. Solar Terr. Phys.*, *66*, 567–572.

Burrage, M., D. Wu, W. Skinner, D. Ortland, and P. Hays (1995), Latitude and seasonal dependence of the semidiurnal tide observed by the high-resolution Doppler imager, *J. Geophys. Res.*, *100*(D6), 11,313–11,321, doi:10.1029/95JD00696.

Copeland, R. A., G. P. Smith, M. M. Mlynczak, and K. S. Kalogerakis (2006), Deactivation of highly vibrationally excited OH by O atoms, *Eos Trans. AGU*, *87*(52), Fall Meet. Suppl., Abstract SA21A-0225.

Evans, W. F. J., I. C. McDade, J. Yuen, and E. J. Llewellyn (1988) A rocket measurement of the O_2 infrared atmospheric (0-0) band emission in the dayglow and a determination of the mesospheric ozone and atomic oxygen densities, *Can. J. Phys.*, *66*, 941–946.

Funke, B., M. Lopez-Puertas, M. Garcia-Comas, G. P. Stiller, T. von Clarmann, M. Höpfner, N. Glatthor, U. Grabowski, S. Kellmann, and A. Linden (2009), Carbon monoxide distributions from the upper troposphere to the mesosphere inferred from 4.7 μm non-local thermal equilibrium emissions measured by MIPAS on Envisat, *Atmos. Chem. Phys.*, *9*, 2387–2411.

Garcia, R. R., T. J. Dunkerton, R. S. Lieberman, and R. A. Vincent (1997), Climatology of the semiannual oscillation of the tropical middle atmosphere, *J. Geophys. Res.*, *102*(D22), 26,019–26,032, doi:10.1029/97JD00207.

Gattinger, R. L., et al. (2010), NO_2 air afterglow and O and NO densities from Odin-OSIRIS night and ACE-FTS sunset observations in the Antarctic MLT region, *J. Geophys. Res.*, *115*, D12301, doi:10.1029/2009JD013205.

Good, R. E. (1976), Determination of atomic oxygen density from rocket borne measurements of hydroxyl airglow, *Planet. Space Sci.*, *24*, 389–395.

Hauchecorne, A., J.-L. Bertaux, F. Dalaudier, J. M. Russell, M. G. Mlynczak, E. Kyrölä, and D. Fussen (2007), Large increase of NO_2 in the north polar mesosphere in January–February 2004: Evidence of a dynamical origin from GOMOS/ENVISAT and SABER/TIMED data, *Geophys. Res. Lett.*, *34*, L03810, doi:10.1029/2006GL027628.

Hecht, J. H., A. Z. Liu, R. L. Walterscheid, R. G. Roble, M. F. Larsen, and J. H. Clemmons (2004), Airglow emissions and oxygen mixing ratios from the photometer experiment on the turbulent oxygen mixing experiment (TOMEX), *J. Geophys. Res.*, *109*, D02S05, doi:10.1029/2002JD003035.

Iwagami, N., T. Shibaki, T. Suzuki, H. Sekiguchi, N. Takegawa, and W. H. Morrow (2003), Rocket observations of atomic oxygen density and airglow emission rate in the WAVE2000 campaign, *J. Atmos. Solar Terr. Phys.*, *66*(16–18), 1349–1360.

Jin, J. J., et al. (2005), Co-located ACE-FTS and Odin/SMR stratospheric-mesospheric CO 2004 measurements and comparison with a GCM, *Geophys. Res. Lett.*, *32*, L15S03, doi:10.1029/2005GL022433.

Kutepov, A. A., A. G. Feofilov, B. T. Marshall, L. L. Gordley, W. D. Pesnell, R. A. Goldberg, and J. R. Russell III (2006), SABER temperature observations in the summer polar mesosphere and lower thermosphere: Importance of accounting for the CO_2 ν_2 quanta V-V exchange, *Geophys. Res. Lett.*, *33*, L21809, doi:10.1029/2006GL026591.

Llewellyn, E. J., and I. C. McDade (1996), A reference model for atomic oxygen in the terrestrial atmosphere, *Adv. Space Res.*, *18*, 209–226.

Llewellyn, E. J., I. C. McDade, P. Moorhouse, and M. D. Lockerbie (1993), Possible reference models for atomic oxygen in the terrestrial atmosphere, *Adv. Space Res.*, *13*, 135–144.

Madronich, S., and S. Flocke (1998), The role of solar radiation in atmospheric chemistry, in*Handbook of Environmental Chemistry*, edited by P. Boule, pp. 1–26, Springer, Heidelberg, Germany.

Manney, G. L., K. Krüger, J. L. Sabutis, S. A. Sena, and S. Pawson (2005), The remarkable 2003–2004 winter and other recent warm winters in the Arctic stratosphere since the late 1990s, *J. Geophys. Res.*, *110*, D04107, doi:10.1029/2004JD005367.

Manney, G. L., et al. (2008), The evolution of the stratopause during the 2006 major warming: Satellite data and assimilated meteorological analyses, *J. Geophys. Res.*, *113*, D11115, doi:10.1029/2007JD009097.

Manney, G. L., M. J. Schwartz, K. Krüger, M. L. Santee, S. Pawson, J. N. Lee, W. H. Daffer, R. A. Fuller, and N. J. Livesey (2009), Aura Microwave Limb Sounder observations of dynamics and transport during the record-breaking 2009 Arctic stratospheric major warming, *Geophys. Res. Lett.*, *36*, L12815, doi:10.1029/2009GL038586.

Marsh, D. R., A. K. Smith, M. G. Mlynczak, and J. M. Russell III (2006), SABER observations of the OH Meinel airglow variability near the mesopause, *J. Geophys. Res.*, *111*, A10S05, doi:10.1029/2005JA011451.

Marsh, D. R., R. R. Garcia, D. E. Kinnison, B. A. Boville, F. Sassi, S. C. Solomon, and K. Matthes (2007), Modeling the whole atmosphere response to solar cycle changes in radiative and geomagnetic forcing, *J. Geophys. Res.*, *112*, D23306, doi:10.1029/2006JD008306.

McDade, I. C., E. J. Llewellyn, and F. R. Harris (1985), Atomic oxygen concentrations in the lower auroral thermosphere, *Adv. Space Res.*, *5*, 229–232.

McDade, I. C., and E. J. Llewellyn (1988), Mesospheric oxygen atom densities inferred from night-time OH Meinel band emission rates, *Planet. Space Sci.*, *36*, 897–905.

McLandress, C., W. E. Ward, V. I. Fomichev, K. Semeniuk, S. R. Beagley, N. A. McFarlane, and T. G. Shepherd (2006), Large-scale dynamics of the mesosphere and lower thermosphere: An analysis using the extended Canadian Middle Atmosphere Model, *J. Geophys. Res.*, *111*, D17111, doi:10.1029/2005JD006776.

Melo, S. M. L., I. C. McDade, and H. Takahashi (2001), Atomic oxygen density profiles from ground-based nightglow measurements at 23°S, *J. Geophys. Res.*, *106*, 15,377–15,384, doi:10.1029/2000JD900820.

Mertens, C. J., M. G. Mlynczak, M. Lopéz-Puertas, P. P. Wintersteiner, R. H. Picard, J. R. Winick, L. L. Gordley, and J. M. Russell III (2001), Retrieval of mesospheric and lower thermospheric kinetic temperature from measurements of CO_2 15 μm Earth limb emission under non-LTE conditions, *Geophys. Res. Lett.*, *28*(7), 1391–1394, doi:10.1029/2000GL012189.

Mertens, C. J., et al. (2004), SABER observation of mesospheric temperature and comparisons with falling sphere measurements taken during the 2002 summer MaCWAVE campaign, *Geophys. Res. Lett.*, *31*, L03105, doi:10.1029/2003GL018605.

Mertens, C. J., et al. (2008), Kinetic temperature and carbon dioxide from broadband infrared limb emission measurements taken from the TIMED/SABER instrument, *Adv. Space Res.*, *43*, 15–27.

Mlynczak, M. G. (1999), A new perspective on the molecular oxygen and hydroxyl airglows emissions, *J. Geophys. Res.*, *104*(D22), 27,535–27,543, doi:10.1029/1999JD000839.

Mlynczak, M. G., D. K. Zhou, and S. M. Adler-Golden (1998), Kinetic and spectroscopic requirements for the inference of chemical heating rates and atomic hydrogen densities from OH Meinel Band measurements, *Geophys. Res. Lett.*, *25*(5), 647–650, doi:10.1029/98GL00325.

Mlynczak, M. G., B. T. Marshall, F. J. Martin-Torres, J. M. Russell III, R. E. Thompson, E. E. Remsberg, and L. L. Gordley (2007), Sounding of the atmosphere using broadband emission radiometry observations of daytime mesospheric $O_2(^1\Delta)$ 1.27 μm emission and derivation of ozone, atomic oxygen, and solar and chemical energy deposition rates, *J. Geophys. Res.*, *112*, D15306, doi:10.1029/2006JD008355.

Nelson, D. D., Jr., A. Schiffman, D. J. Nesbitt, J. J. Orlando, and J. B. Burkholder (1990), H + O_3 Fourier-transform infrared emission and laser absorption studies of OH($X^2\Pi$) radical: An experimental dipole moment function and state-to-state Einstein *A* coefficients. *J. Chem. Phys.*, *93*, 7003–7019.

Oberheide, J., D. Offermann, J. M. Russell III, and M. G. Mlynczak (2006), Intercomparison of kinetic temperature from 15 μm CO_2 limb emissions and OH*(3,1) rotational temperature in nearly coincident air masses: SABER, GRIPS, *Geophys. Res. Lett.*, *33*, L14811, doi:10.1029/2006GL026439.

Offermann, D. (1972), On the atomic oxygen measurements by rocket-borne mass spectrometers, *J. Geophys. Res.*, *77*(31), 6284–6286, doi:10.1029/JA077i031p06284.

Offermann, D., and A. Drescher (1973), Atomic oxygen densities in the lower thermosphere as derived from in situ 5577-A night airglow and mass spectrometer measurements, *J. Geophys. Res.*, *78*(28), 6690–6700, doi:10.1029/JA078i028p06690.

Pancheva, D., P. Mukhtarov, and B. Andonov (2009) Global structure, seasonal and interannual variability of the migrating semidiurnal tide seen in the SABER/TIMED temperatures (2002–2007), *Ann. Geophys.*, *27*, 687–703.

Picone, J. M., A. E. Hedin, D. P. Drob, and A. C. Aiken (2002), NRLMSIS-00 empirical model of the atmosphere: Statistical comparisons and scientific issues, *J. Geophys. Res.*, *107*(A12), 1468, doi:10.1029/2002JA009430.

Randall, C. E., et al. (2005), Stratospheric effects of energetic particle precipitation in 2003–2004, *Geophys. Res. Lett.*, *32*, L05802, doi:10.1029/2004GL022003.

Randall, C. E., V. L. Harvey, D. E. Siskind, J. France, P. F. Bernath, C. D. Boone, and J. U. Kozyra (2006), Enhanced NO_x in 2006 linked to strong upper stratospheric Arctic vortex, *Geophys. Res. Lett.*, *33*, L18811, doi:10.1029/2006GL027160.

Randall, C. E., V. L. Harvey, C. S. Singleton, P. F. Bernath, C. D. Boone, and K. A. Walker (2009), NO_x descent in the Arctic middle atmosphere in early 2009, *Geophys. Res. Lett.*, *36*, L18811, doi:10.1029/2009GL039706.

Remsberg, E. E., et al. (2008), Assessment of the quality of the Version 1.07 temperature-versus-pressure profiles of the middle atmosphere from TIMED/SABER, *J. Geophys. Res.*, *113*, D17101, doi:10.1029/2008JD010013.

Russell, J. M., III, M. G. Mlynczak, L. L. Gordley, J. Tansock, and R. Esplin (1999), An overview of the SABER experiment and preliminary calibration results, *Proc. SPIE Int. Soc. Opt. Eng.*, *3756*, 277–288.

Russell, J. P., and R. P. Lowe (2003), Atomic oxygen profiles (80–94 km) derived from Wind Imaging Interferometer/Upper Atmospheric Research Satellite measurements of the hydroxyl airglow: 1. Validation of technique, *J. Geophys. Res.*, *108*(D21), 4662, doi:10.1029/2003JD003454.

Russell, J. P., R. P. Lowe, and W. E. Ward (2004), Atomic oxygen annual and semiannual variations in the mesopause region for mid and equatorial latitudes, *J. Atmos. Solar Terr. Phys.*, *66*, 451–461.

Russell, J. P., W. E. Ward, R. P. Lowe, R. G. Roble, G. G. Shepherd, and B. Solheim (2005), Atomic oxygen profiles (80 to 115 km) derived from Wind Imaging Interferometer/Upper Atmospheric Research Satellite measurements of the hydroxyl and greenline airglow: Local time latitude dependence, *J. Geophys. Res.*, *110*, D15305, doi:10.1029/2004JD005570.

Sander, S. P., et al. (2006), Chemical kinetics and photochemical data for use in stratospheric modeling, Evaluation 15, *JPL Publ.*, *06-2*, 523 pp.

Shepherd, G. G., et al. (1993), Longitudinal structure in atomic oxygen concentrations observed with WINDII on UARS, *Geophys. Res. Lett.*, *20*(12), 1303–1306, doi:10.1029/93GL01105.

Siskind, D. E., S. D. Eckermann, L. Coy, J. P. McCormack, and C. E. Randall (2007), On recent interannual variability of the Arctic winter mesosphere: Implications for tracer descent, *Geophys. Res. Lett.*, *34*, L09806, doi:10.1029/2007GL029293.

Smith, A. K., and D. R. Marsh (2005), Processes that account for the ozone maximum at the mesopause, *J. Geophys. Res.*, *110*, D23305, doi:10.1029/2005JD006298.

Smith, A. K., D. R. Marsh, and A. C. Szymczak (2003), Interaction of chemical heating and the diurnal tide in the mesosphere, *J. Geophys. Res.*, *108*(D5), 4164, doi:10.1029/2002JD002664.

Smith, A. K., D. R. Marsh, J. M. Russell III, M. G. Mlynczak, F. J. Martin-Torres, and E. Kyrölä (2008), Satellite observations of high nighttime ozone at the equatorial mesopause, *J. Geophys. Res.*, *113*, D17312, doi:10.1029/2008JD010066.

Smith, A. K., M. Lopéz-Puertas, M. García-Comas, and S. Tukiainen (2009) SABER observations of mesospheric ozone during NH late winter 2002–2009. *Geophys. Res. Lett.*, *36*, L23804, doi:10.1029/2009GL040942.

Spencer, J. E., and G. P. Glass (1977), Some reactions of OH(v = 1), *Int. J. Chem. Kinet.*, *9*, 111–122.

van der Loo, M. P. J., and G. Groenenboom (2007), Theoretical transition probabilities for the OH Meinel band system, *J. Chem. Phys.*, *126*, 114314, doi:10.1063/1.2646859.

von Zahn, U., J. Höffner, V. Eska, and M. Alpers (1996), The mesopause altitude: Only two distinctive levels worldwide?, *Geophys. Res. Lett.*, *23*(32), 3231–3234, doi:10.1029/96GL03041.

Winick, J. R., P. P. Wintersteiner, R. H. Picard, D. Esplin, M. G. Mlynczak, J. M. Russell III, and L. L. Gordley (2009), OH layer characteristics during unusual boreal winters of 2004 and 2006, *J. Geophys. Res.*, *114*, A02303, doi:10.1029/2008JA013688.

Xu, J., H.-L. Liu, A. K. Smith, R. G. Roble, C. J. Mertens, J. M. Russell III, and M. G. Mlynczak (2007), Mesopause structure from Thermosphere,

Ionosphere, Mesosphere, Energetics and Dynamics (TIMED)/Sounding of the Atmosphere using Broadband Emission Radiometry (SABER) observations, *J. Geophys. Res.*, *112*, D09102, doi:10.1029/2006JD007711.

Xu, J., A. K. Smith, H.-L. Liu, W. Yuan, Q. Wu, G. Jiang, M. G. Mlynczak, J. M. Russell III, and S. J. Franke (2009), Seasonal and quasi-biennial variations in the migrating diurnal tide observed by Thermosphere, Ionosphere, Mesosphere, Energetics and Dynamics (TIMED), *J. Geophys. Res.*, *114*, D13107, doi:10.1029/2008JD011298.

Zhu, X., J.-H. Yee, and E. R. Talaat (2007), Effect of dynamical-photochemical coupling on oxygen airglow emission and implications for daytime ozone retrieved from 1.27 μm emission, *J. Geophys. Res.*, *112*, D20304, doi:10.1029/2007JD008447.

D. R. Marsh and A. K. Smith, Atmospheric Chemistry Division, National Center for Atmospheric Research, PO Box 3000, Boulder, CO 80307, USA. (aksmith@ucar.edu)

J. C. Mast, Science Systems and Applications Inc., Hampton, VA 23666, USA.

M. G. Mlynczak, NASA Langley Research Center, Hampton, VA 23681, USA.